nature communications

Article

https://doi.org/10.1038/s41467-025-57523-0

Retention of high-pressure solution-processable metastable phase to ambience via differential sublattice rigidity for broadband photodetectors

Received: 11 October 2024

Accepted: 24 February 2025

Zhongyang Li[1,2,10], Jue Gong[3,10], Zhikai Zhu[1], Donghao Liu[4], Qingyang Hu[1], Yiming Wang[1], Xuqiang Liu[1], Shuo Zhou[1,4], Hui Luo[1], Dong Wang[1], Xingyi Liu[3], Zengxi Yang[3], Min Tang[3], Qingyu Kong[5], N-Diaye Adama[5], Kai Zhang[1,5], Shuai Yan[6], Lili Zhang[6], Xiaohui Zeng[2], Zhenhai Yu[2], Wei Xia[2,7], Jian Yuan[2], Mingtao Li[1], Nana Li[1], Hongliang Dong[1], Ziyou Zhang[1], Haiyun Shu[1], Yang Ding[1], Dongbo Wang[4], Yanfeng Guo[2,7], Tao Xu[8], Lingping Kong[1] ✉, Wenge Yang[1], Ho-kwang Mao[1,9] & Gang Liu[1,9] ✉

Materials science exploits only properties that are available at ambience. Therefore, although high-pressure changes the physical state of all condensed matter, most of the extraordinary properties discovered vanish after decompression and cannot be utilized. Here, we demonstrate sublattice decoupling in a mixed-anion chalcohalide $Rb_6Re_6S_8I_8$ upon compression, in which the $[Rb_6I_2]^{4+}$ framework is soft and plastic, while the $[Re_6S_8I_6]^{4-}$ clusters are hard and elastic. This discrepancy in the rigidity allows the applied pressure to selectively amorphize the framework while maintaining the ordered state in the cluster, leading to intriguing photocurrent generation and enhancement upon compression. These high-pressure properties are retained at ambience, permitting scalable synthesis of the decompressed samples using a large-volume press, followed by further fabrication into self-powered broadband photodetectors with a response time of ~ 10^2 μs and a specific detectivity of ~ 10^{11} Jones. This study subverts the stereotype that pressure engineering is hardly to be employed for device applications.

Using pressure to manipulate the physical state of condensed matter is as fundamental as changing temperature or tuning chemical composition for the same purpose[1]. Therefore, pressure is a distinctive dimension for seeking improved or even unprecedented properties in compressed materials, as evidenced by numerous reports on metallic hydrogen, high-temperature superconductors, photovoltaic semiconductors, and so on[2–6]. However, retaining and utilizing properties attainable at high pressure for ambient applications has been

---

[1]Center for High Pressure Science and Technology Advanced Research (HPSTAR), Shanghai, China. [2]School of Physical Science and Technology (SPST), ShanghaiTech University, Shanghai, China. [3]Sichuan University-Pittsburgh Institute, Sichuan University, Chengdu, China. [4]School of Materials Science and Engineering, Harbin Institute of Technology, Harbin, China. [5]Synchrotron SOLEIL, L'Orme des Merisiers Saint-Aubin, Gif-sur-Yvette, France. [6]Shanghai Institute of Applied Physics, Chinese Academy of Sciences, Shanghai, China. [7]ShanghaiTech Laboratory for Topological Physics, ShanghaiTech University, Shanghai, China. [8]Department of Chemistry and Biochemistry, Northern Illinois University, DeKalb, IL, USA. [9]Shanghai Key Laboratory of Material Frontiers Research in Extreme Environments (MFree), Shanghai Advanced Research in Physical Sciences (SHARPS), Shanghai, China. [10]These authors contributed equally: Zhongyang Li, Jue Gong. ✉e-mail: konglp@hpstar.ac.cn; liugang@hpstar.ac.cn

challenging because of the degradation of the high-pressure-induced properties after decompression and the inevitable trade-off between sample quantity and the magnitude of attainable pressure[7,8].

Two strategies have been proposed to overcome this formidable obstacle. In the first approach, inspired by natural mineral inclusions[9–11], nanostructured diamond capsules (NDCs) have been developed to confine samples and preserve their high pressure-induced properties[12]. However, man-made NDCs can encapsulate only gaseous and volatile samples because of their softness and compressibility. In addition, this technique requires high temperatures to convert graphite to diamond for in situ preservation of target materials, thus showing limited applicability for organics or materials with low decomposition temperature. Moreover, after decompression, the target material is isolated in nanostructured diamond and forbidden to form a pure material, thus impeding contact-based material analysis or large-scale device applications. Another route is to engineer the kinetic barriers in the phase transformation to obtain ambient-pressure metastable materials[13–15]. This method has been realized in specific nanomaterials with interconnected nanocrystal networks[13]. However, no device applications using such metastable materials have been reported to date.

A potential opportunity for ambient retention of high pressure-induced properties lies in tailoring the coupling between sublattices. Conventionally, a sublattice is a simple mathematical concept related to a subset of the translations of a lattice[16]. Sublattice modeling has now been extensively adopted to describe a variety of materials, ranging from alloys to ionic liquids[17,18]. All of these successful studies indicate that the sublattices in these systems are strongly coupled through their structural periodicity; thus, their responses under stimuli should be synchronized. By contrast, if the material is designed such that individual sublattices are weakly coupled through non-chemical bonding and a large discrepancy in the rigidity is present between various sublattices, pressure can be used to decouple the structural periodicity. More importantly, the properties acquired at high pressure become irreversibly frozen during decompression because of the nonsynchronized structural changes between the sublattices.

Very recently, the $Rb_6Re_6S_8I_8$ chalcohalide inorganic compound has been reported[19], which is structurally characterized by two sublattices: the $[Re_6S_8I_6]^{4-}$ (Re-S-I(1)) cluster and the $[Rb_6I_2]^{4+}$ (Rb-I(2)) electrostatic framework. These two sublattices are mutually coupled by electrostatic attraction forces that are significantly weaker than those of chemical bonds. At ambient pressure, this material shows strong photoluminescence (PL) but does not exhibit a photocurrent response. However, upon compression, there is a significant pressure-generated photocurrent in this material, which is retained at ambient pressure after the applied pressure is completely removed. As a proof for device application, a large-volume press (LVP) is employed to pressurize and depressurize a scalable quantity of $Rb_6Re_6S_8I_8$ inheriting the pressure-induced photoelectric properties. This material is then used to build ambience-operational photodetectors. Notable photocurrent responses are observed under excitation by both ultraviolet and visible light. These results, together with the elucidated thermodynamic and kinetic mechanisms, enable high-pressure properties to be employed in optoelectronics that must operate under ambient conditions.

Results and discussion

Discovery of differential sublattice rigidity

We first prepared high-quality $Rb_6Re_6S_8I_8$ single crystals (Supplementary Fig. 1 and Supplementary Table 1). As revealed by a combination of in situ high-pressure structural characterizations (Fig. 1), the rigidities of two sublattices, the $[Re_6S_8I_6]^{4-}$ cluster and the $[Rb_6I_2]^{4+}$ framework, are significantly different. Owing to lattice shrinkage, the high-pressure X-ray diffraction (XRD) pattern implies monotonic shifts of Bragg reflections towards larger 2θ angles from 1 atm to ~10–12 GPa, above which the pattern becomes diffusive for lattice distortion, and the structure cannot maintain long-range ordered atomic arrangements (Fig. 1a). Using GSAS software, we extract the pressure dependence of interatomic distances, where the framework-related Rb-Rb, Rb-I(1) and Rb-I(2) undergo monotonic distance reductions, yet the cluster-related bond lengths of Re-I(1), Re-Re and Re-S, as well as the I(1)-Re-S, S-Re-S and Re-S-Re bond angles, are nearly unchanged; thus, the clusters remain undisturbed at higher pressures (Fig. 1b, c, and Supplementary Figs. 2 and 3), and the root cause of amorphization is the collapse of the Rb-I(2) framework.

The hard rigidity of the cluster sublattice is further supported by the results of two independent experiments, namely high-pressure Raman spectroscopy (Supplementary Fig. 4) and X-ray absorption spectroscopy (XAS) (Supplementary Fig. 5). According to the calculated results of the vibrational mode assignment, all of the initial Raman modes are based on the cluster rather than on the framework. The pressure dependence of the Raman spectra clearly shows that these modes are distinguished up to 20 GPa (Fig. 1d), with no noticeable increase in the full width at half maximum (FWHM) (Fig. 1e), showing short-range order characteristics. Such sharp modes exhibit a sustained blueshift, even after the process of amorphization is completed, as revealed by XRD (Fig. 1a), demonstrating a specific decoupling between long-range crystalline disorder and short-range local order. Using XAS as another quantitative validation tool, it is observed that the edge energy (E_0) and line energy (E_w), which are defined by the peaks of the first and second derivatives of $\mu(E)$, respectively, remain constant at ~10.537 keV and ~10.539 keV as the pressure increases (Fig. 1f, g), indicating that there is no change in the valence state or coordination environment of Re. This pressure independence of the energy position reflects the robust nature of the Re-S-I cluster. Furthermore, the Fourier transform magnitude of the XAS spectra suggests that the Re-S interatomic distance does not vary significantly (Fig. 1h and i), again verifying the nonsynchronous lattice disorder processes and the difference in rigidity between cluster-structured $[Re_6S_8I_6]^{4-}$ and electrostatic $[Rb_6I_2]^{4+}$ sublattices. The difference in the compressibility between the cluster and electrostatic frameworks provides a structural basis for the adjustable and irreversible optical and electronic properties discussed below.

Pressure-induced emission transitions

We then focused on the high-pressure-driven functional response of $Rb_6Re_6S_8I_8$. The different compressibility of the Re-S-I(1) cluster and the Rb-I(2) electrostatic framework can lead to attenuated photoluminescence (PL) but also an emergent photocurrent response of $Rb_6Re_6S_8I_8$. As shown in Fig. 2a and Supplementary Fig. 6, while pressure-dependent PL generally results in a reduction in the emission intensity at higher pressures, slight increases in the PL intensity and prolongation of the carrier lifetime are observed at a mild pressure of ~0.1 GPa (Fig. 2b–g; Supplementary Figs. 7–9). On the other hand, the PL peak wavelength displays a monotonic blueshift with increasing pressure (Fig. 2c), which is in contrast to the trend observed for the pressure-dependent UV-Vis absorbance. In addition, the full width at half maximum (FWHM) of the PL spectra also decreases with increasing pressure (Fig. 2d), which is additionally corroborated by the second central moment (m_2), which also displays a similar decreasing trend (Fig. 2e), indicating that the energy density of states increases upon compression[20]. We also note that the PL annihilation is associated with the shortened PL lifetimes upon compression (Fig. 2f, g).

The PL properties and exciton/carrier dynamics of similar compounds are highly dependent on the properties of structurally isolated clusters[20–22], and the lifetime is strongly affected by ligands of rhenium. Upon compression, hydrostatic pressure first compresses the Rb-I(2) electrostatic framework owing to its much softer nature, with the

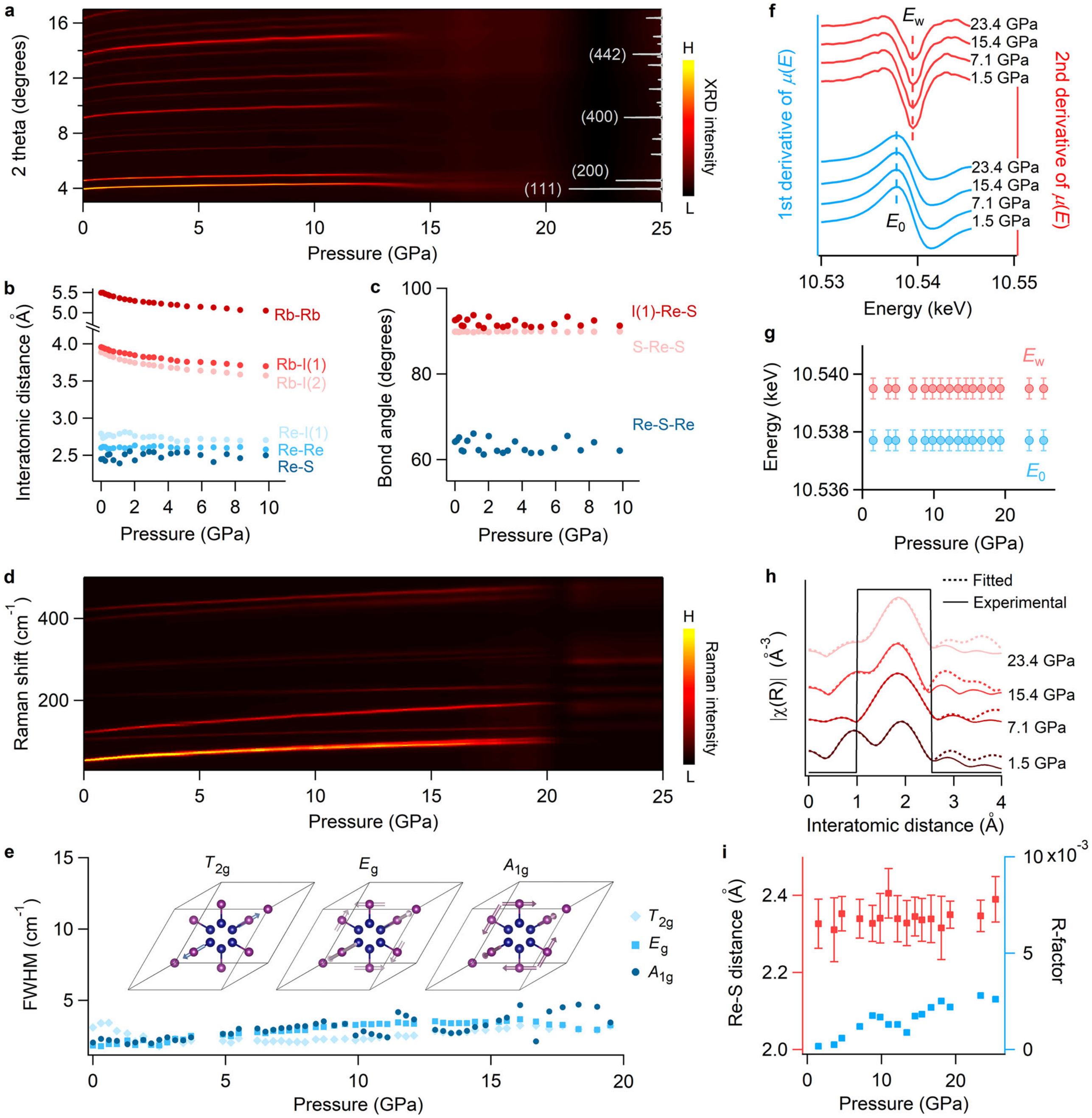

Fig. 1 | Structural evolutions of $Rb_6Re_6S_8I_8$ upon compression. a Pressure-dependent in situ synchrotron-based XRD pattern, showing structural amorphization starting at ~12 GPa. The XRD pattern collected at ambient pressure is highlighted in gray, and indicates that no crystalline phase transition occurred prior to amorphization. **b** and **c** Evolution of the interatomic distance and bond angles under pressure, suggesting differential rigidity. We identify two distinct compression behaviors dominated by the significantly soft Rb-I(2) framework and the cage-structured Re-S-I(1) sublattice that is extremely insensitive to pressure. **d** Pressure dependence of the Raman spectra upon compression. **e** Pressure dependence of the full width at half maximum (FWHM) of the representative Raman modes, which are nearly unchanged upon compression. **f** First and second derivatives of the Re L_3 edge $\mu(E)$ plotted versus the photon energy of $Re_6Rb_6S_8I_8$ at different pressures upon compression. **g** Constant edge energy (E_0) and white line energy (E_w) during the investigated compression process. **h** Pressure dependence of the XAS Fourier transform magnitude as a function of interatomic distance and fittings based on nearest neighbor (Re-S) at selected pressures. **i** Fitted interatomic Re-S distance. The low R-factors, which are on the order of 10^{-4} show the high goodness of fit. During the whole compression process up to 25.4 GPa, no obvious change occurs in the interatomic distance within the $[Re_6S_8I_6]^{4-}$ cluster. The error bars in (**g** and **i**) denote the fitting errors.

compressed Rb-I(2) framework eventually tuning atomic connections within the Re-S-I(1) cluster structure. Then, the original crystal field of the Re-S-I(1) cluster is modified due to the perturbed electron clouds of the S/I ligands under lattice compression. Therefore, PL attenuation at higher pressures can be considered the result of increased long-range interactions between the Re-S-I(1) cluster and the Rb-I(2) framework. This process is critically influenced by spin-spin interactions, which are governed by the Ruderman-Kittel-Kasuya-Yosida (RKKY) interaction and further modulated by crystal field effects[23,24].

To delve deeper into the mechanisms underlying emission transitions, we investigate the role of self-trapped excitons (STEs). In crystalline materials, excitons interact with phonons via electron-phonon coupling. When this coupling is weak, excitons are primarily scattered by phonons. In contrast, strong coupling can lead to the self-

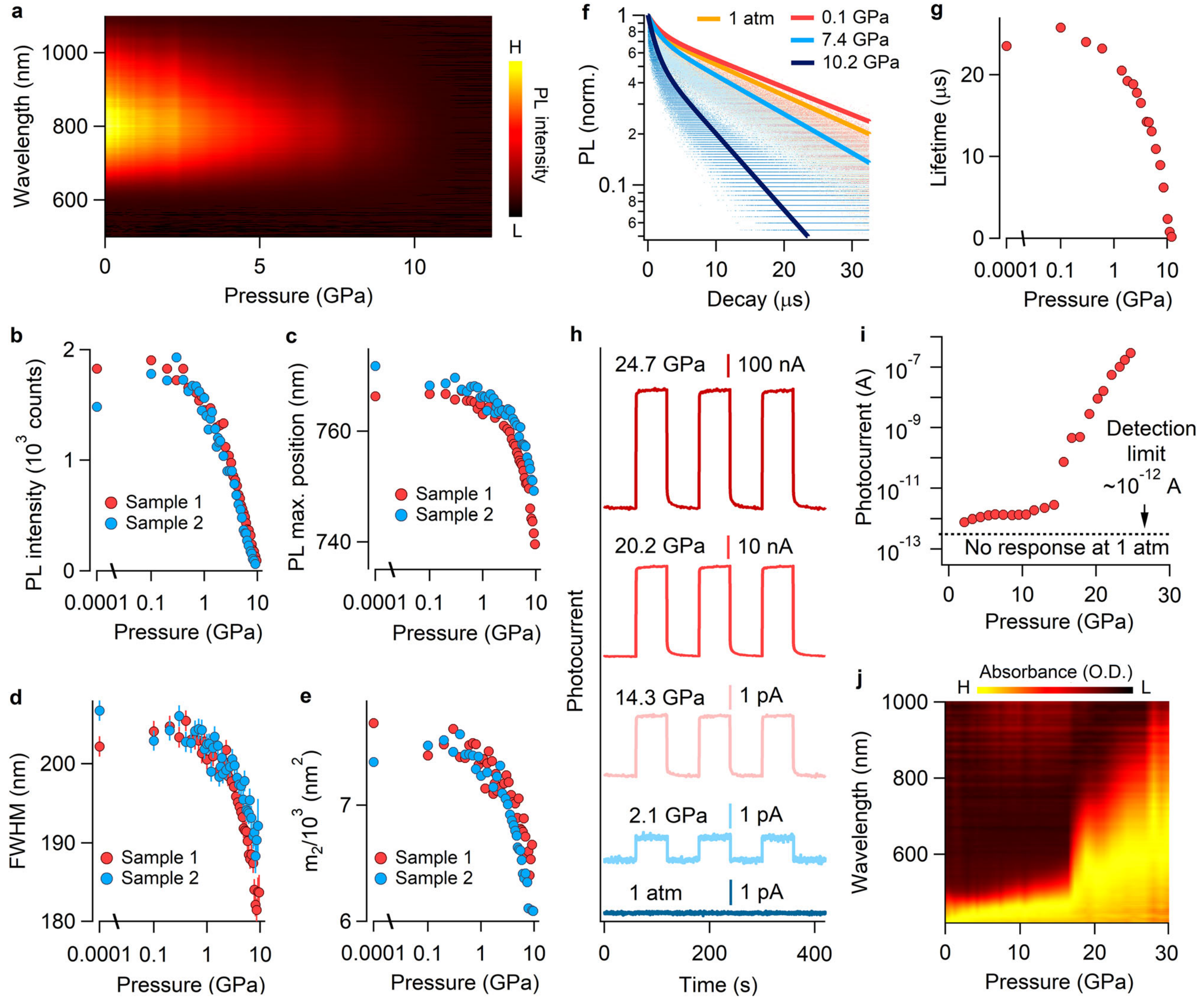

Fig. 2 | Pressure-dependent optical properties of $Rb_6Re_6S_8I_8$ during compression. **a** Pressure-dependent PL contour plot from 1 atm to 12 GPa, where the PL emission is fully annihilated. **b**–**e** Pressure dependences of the PL intensity, PL peak wavelength, and full width at half maximum (FWHM) of the PL peak and second central moments (m_2), respectively. Here, for a Gaussian-type emission profile, the FWHM is conveniently quantified by m_2 as $m_2 = (\mathrm{FWHM})^2/8\ln 2$, where the error bar in **d** shows the fitting errors. Note that two individual samples, 1 and 2, were employed to confirm the validity of the experimental results. **f** Experimental time-resolved PL decays (dots) and fittings (solid lines) from 1 atm to 10.2 GPa. **g** The extracted carrier lifetimes obtained by fitting the time-resolved PL decay traces in **f**. **h** Comparison of the on-off photocurrent response and magnitudes from 1 atm to 24.7 GPa. **i** Evolution of the photocurrents extracted from (**h**). **j** Pressure-dependent UV-vis absorbance near bandgap regions from 1 atm to 30 GPa, where a drastic narrowing of the bandgap can be observed at approximately 17 GPa. Therefore, the onset pressures for abrupt bandgap narrowing, drastic photocurrent increase, and long-range disorder are coincident, thus indicating that structural amorphization is the common origin for the property changes. The sizes of the symbols shown in (**b**, **c**, **e**, **g** and **i**)cover the experimental or fitting errors.

trapping of excitons. Specifically, an STE is formed because photo-induced local lattice distortion occurs due to strong electron-phonon coupling[25]. For the studied $Rb_6Re_6S_8I_8$ material, the broad sub-bandgap emission with a large Stokes shift observed at ambience is the fingerprint of the STE. Two additional pieces of evidence further support the existence of STEs in $Rb_6Re_6S_8I_8$: 1) Soft lattice. According to the XRD results shown in Supplementary Fig. 2, the bulk modulus of $Rb_6Re_6S_8I_8$ is ~11 GPa, which is significantly lower than that of the conventional semiconductor Si and even lower than that of organic-inorganic hybrid perovskites (~ 15–20 GPa)[26]. This soft lattice is conducive to lattice deformation, which is crucial for the formation of an STE[27]. 2) Low electronic dimensionality. From the calculated band structure results shown in Supplementary Fig. 10, we observe flat conduction bands (CBs) and valence bands (VBs), indicating localized zero-dimensional features. Such low electronic dimensionality is a prerequisite for the formation of STEs[28]. For excitons to become self-trapped, neither photogenerated electrons nor holes, or both, can exhibit high delocalization; that is, the effective mass of at least one carrier must be sufficiently high. In other words, low electronic dimensionality, which reflects the extent of orbital overlap, is essential for the formation of STEs and, consequently, for broadband emission.

All of these observations demonstrated that STE is the origin of broad PL, and we can see that the evolution of STEs controls the emission transitions observed at pressures. Upon compression, the STE in $Rb_6Re_6S_8I_8$ is suppressed and weakened, which can be easily understood from the fact that its lattice becomes more rigid at higher pressure; therefore, photoinduced local lattice distortion and electron-phonon coupling become difficult. This argument is also supported by the reduced FWHM of the PL spectra upon increased pressure, as shown in Fig. 2d, indicating that the STE feature is weakened at high pressure. In addition, we further studied the pressure-dependent self-trapping energy (E_{st}), which is estimated as $E_{st} = E_g - E_{PL}$, where E_g is the bandgap energy, and E_{PL} is the PL emission energy. In the studied material, rhenium chalcohalide clusters are completely isolated by the large $[Rb_6I_2]^{4+}$ framework, forming a nominal 0D structure, as confirmed by our band-structure calculations (Supplementary Fig. 10). In 0D systems, the energy barrier between the free exciton and STE is considered not to exist[27,29]. We also note that the VB of this material is flat, particularly at low pressure, so that the lattice deformation energy should be very small. Supplementary Fig. 11 shows the pressure-dependent bandgap energy and PL energy upon compression, from which it is observed that from ambient pressure to 10 GPa, the bandgap energy is first relatively stable, and then decreases, while the PL energy increases monotonically. Therefore, we can conclude that a reduction of E_{st}, rendering the STE unstable; this implies that the STE cannot act as an effective PL mechanism at high pressures.

Pressure-induced photocurrent generation and enhancement

The pressure-induced photocurrent transitions, where the STE again plays a crucial role, are of particular interest. As shown in Fig. 2h and i, we can identify two stages of the evolution of the pressure-induced photocurrent. The first stage is the initial photocurrent generation occurring at ~2 GPa, prior to which the photocurrent is undetectable. The second stage occurs at ~15 GPa, after which the photocurrent is greatly enhanced upon compression. The self-trapping energy describes the extent of binding of the STE. Therefore, the reduced E_{st} of $Rb_6Re_6S_8I_8$ at higher pressures facilitates the dissociation of STEs into free carriers. From the calculated band structure (Supplementary Fig. 10), one can expect that owing to the fluctuation of the VB at higher pressure, the effective mass will decrease upon compression, leading to enhanced carrier mobility. Then, the pressure-induced greater mobility allows these free carriers to more easily migrate towards the current-collecting electrodes of the photodetector devices. Therefore, a detectable photocurrent is achieved via pressure-reduced excitonic behavior at ~2 GPa.

For the pressure-enhanced photocurrent above ~15 GPa, the increasing trend of the photocurrent agrees well with the redshift in the optical bandgap (Fig. 2j; Supplementary Figs. 12–15), indicating their common structural origin. Structurally, compression results in amorphization, causing the formation of a chemical bond between Rb and I(2) that originally interacted through Coulomb attraction. This argument can be verified by extending the graph of the Rb-I(2) interatomic distance (Fig. 1b) to a higher pressure, e.g., 15 GPa, from which a 3.6 Å interatomic distance that is very close to the Rb-I ionic bond length (3.66 Å) can be extracted. Thus, it is reasonably believed that there is a high probability that Rb-I forms chemical bonds in $Rb_6Re_6S_8I_8$ within the pressure range beyond 15 GPa; this facilitates an electron transition from the VB to the CB, thereby dramatically narrowing the optical bandgap. The higher carrier density therefore leads to a photocurrent enhancement of over three orders of magnitude within the 15–20 GPa pressure range.

Irreversible structural transition

In addition to the different compression behaviors of the Re-S-I(1) cluster and the Rb-I(2) framework, these two structural moieties also exhibit distinct irreversibility after decompression, and the ambient structure of the recovered sample is strongly associated with the peak applied pressure (Fig. 3; Supplementary Figs. 16–19). Generally, $Rb_6Re_6S_8I_8$ shows long-range disorder as it is decompressed from higher peak pressures, rendering it amorphous without structural robustness (Fig. 3a). The ambient structures of the as-synthesized $Rb_6Re_6S_8I_8$ sample and the $Rb_6Re_6S_8I_8$ among samples decompressed from different peak pressures were further compared using in situ Raman spectroscopy (Fig. 3b). For the samples decompressed from 25 GPa, distinctive modes are clearly shown, suggesting an ordered Re-S-I(1) cluster structure. Nonetheless, even for the sample that underwent high-pressure treatment and then was decompressed from a relatively lower peak pressure of 18 GPa, the XRD pattern already clearly shows a disordered long-range structure (Fig. 3a). This phenomenon indicates the different structural reversibility of the Re-S-I(1) cluster and the Rb-I(2) framework.

Therefore, one can visualize a decoupled Re-S-I(1) cluster and Rb-I(2) framework, where the former component is mechanically more resilient to pressure and does not affect structural periodicity to a large extent, whereas Rb-I(2) is spatially widespread, and directly regulates the long-range order of the $Rb_6Re_6S_8I_8$ lattice; this means that structural plasticity exists in $Rb_6Re_6S_8I_8$, which is dictated by the least irreversible recovery of the Rb-I(2) framework from the high-pressure treatment cycle. Furthermore, by fitting the Fourier transformed XAS magnitude with the nearest neighbor (Re-S), it was revealed that after the compression-decompression cycle with a peak pressure of 25 GPa, the bond length of Re-S was 2.27 Å, showing only negligible deviation from the 2.33 Å Re-S bond length obtained with a peak pressure of 1.5 GPa (Fig. 3c). Figure 3d shows the structural evolution of the Re-S-I(1) cluster and the Rb-I(2) framework before and after high-pressure treatment. The structural irreversibility therein gives rise to a permanent modification of functional properties, which is promising for engineered device design. We also note that even after the compression-decompression cycle with a low peak-pressure of 2 GPa, although no phase transition is observed, the microstructure of $[Re_6S_8I_6]^{4-}$ is irreversibly modified, leading to a PL enhancement (Supplementary Fig. 16).

Pressure-cycle-induced photocurrent retainable at ambience

Benefiting from irreversible structural transitions, recovered $Rb_6Re_6S_8I_8$ retains its high-pressure properties that depend on the magnitude of peak applied pressure (Supplementary Figs. 20–23). Specifically, it even exhibits monotonically increased photocurrents with larger number of compression-decompression cycles (Fig. 4a). To explore the structural origin of the retained photocurrents at ambience, we conducted molecular dynamics simulations of the mean squared distances (MSDs) of the Rb, I, S, and Re atoms and observed more intensive fluctuations in the Rb-Rb distance as a function of simulation time, indicating that the polarizability and plasticity of the framework atoms are much greater than those of the other structural components (Fig. 4b; Supplementary Fig. 24). The larger deformability of the Rb-I(2) framework thereby explains the observed drastic bandgap redshift occurring at 17 GPa (Fig. 2j) along with the concomitant photocurrent enhancement (Fig. 2i).

We also compared the bandgap difference between the initial state of the materials before compression and the decompressed state from high-pressure cycles, with the data shown in Supplementary Fig. 20. It is observed that the optical bandgap cannot recover to the magnitude before compression; however, it exhibits a redshift after the first compression-decompression cycle and another redshift after the second cycle. Additionally, it is observed from the pressure dependence of the Urbach energy upon compression-decompression cycles that prior to the compression-decompression cycles, the absorbance curve exhibits a sharper profile, indicating a relatively ordered structure, whereas after the compression-decompression cycles, there is a significant increase in the magnitude of the Urbach energy, indicating a more disordered structure (Supplementary Fig. 20)[30]. All of these results are consistent with the argument that amorphization disorder plays a crucial role in photocurrent enhancement at high-pressure region over 15 GPa. In addition, the magnitude of the self-trapping energy can be estimated by the difference between the bandgap energy and the emission energy. Considering that the emission energy recovers to the initial state before compression (Supplementary Fig. 21), we can conclude that the self-trapping energy decreases after pressure treatment because the bandgap redshifts, meaning that the STE becomes unstable, leading to PL quenching (Supplementary Fig. 21) and the generation of photocurrent due to the dissociation of the STEs into free carriers.

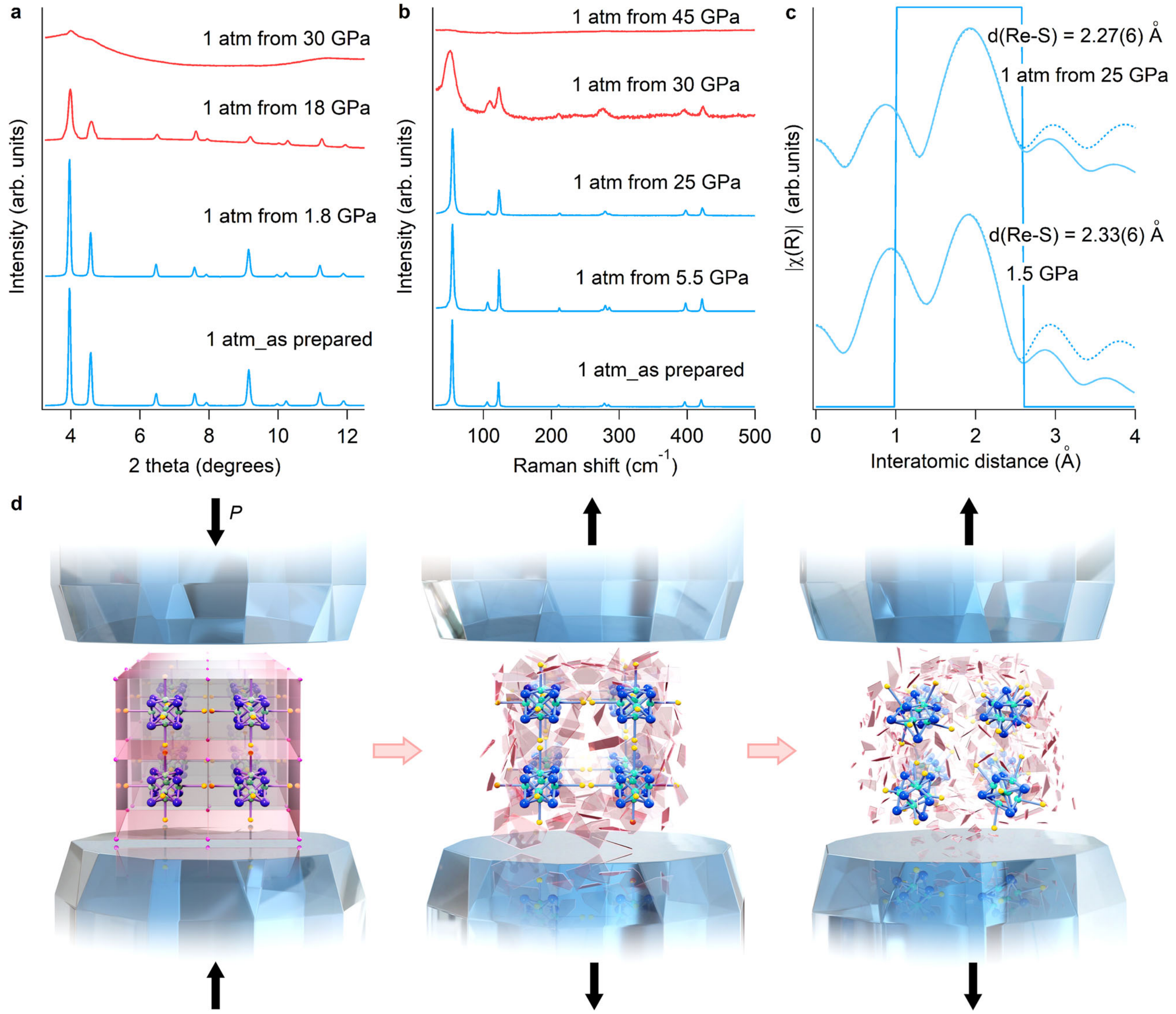

Fig. 3 | Compression-decompression dependent structural transitions of $Rb_6Re_6S_8I_8$. **a** XRD patterns of samples of powders ground from the as-prepared crystal and samples recovered from different peak pressures. **b** Raman spectra of samples of powders ground from the as-prepared crystal and samples recovered from different peak pressures. **c** XAS Fourier transform magnitudes as a function of interatomic distance and fittings (dashed line) based on nearest neighbor (Re-S) at ambient pressure as recovered from 1.5 GPa and 25 GPa peak pressures. **d** Schematic illustration of hydrostatic compression of $Rb_6Re_6S_8I_8$, which leads to nonsynchronous lattice disorder of the $[Re_6S_8I_6]^{4-}$ cluster and the Rb-I electrostatic framework, also showing the plasticity of the Rb-I framework, resulting in incomplete recovery from the high-pressure disorder state. The nonsynchronous amorphization processes of the Re-S-I(1) and Rb-I(2) sublattices, along with their different extents of recrystallization, indicate the irreversibility of high-pressure amorphization.

Scalable decompressed sample for device fabrication

To demonstrate the practical device applicability of the photocurrent enhancement, we use a large volume press (LVP) to prepare large-scale samples with high-pressure treatment (Fig. 4c). The sample pressure-treated under LVP was then fabricated into a Schottky-type Pt/$Rb_6Re_6S_8I_8$/Pt photodetector on a substrate (Fig. 4d), by taking the advantage of the good solution processability of the decompressed samples. Figure 4e shows the picture of N,N-dimethylformamide (DMF) solution of decompressed $Rb_6Re_6S_8I_8$ sample, from which one can see the sample is totally dissolved in DMF solvent. We further let the solvent evaporate to induce a recrystallization of $Rb_6Re_6S_8I_8$, and conducted XRD experiment on this sample. Although structural diffraction results in identifiable Bragg peaks, it shows rather diffusive background in the XRD pattern (Supplementary Fig. 25a), thus indicating a partially amorphous nature of the solution-processed sample, confirming the metastable phase is preserved. Here, the rubidium iodide ($[Rb_6I_2]^{4+}$) framework is stable in DMF, rather than behaving as Rb^+ and I^-, which can be understood by the effect of ion association. Such a demonstration is further supported by the study of particle size in DMF solvent. We conducted dynamic light scattering (DLS) experiments on three samples in DMF with the same mol% concentration: as-prepared $Rb_6Re_6S_8I_8$; large volume press (LVP)-treated $Rb_6Re_6S_8I_8$, and RbI. Supplementary Fig. 25b shows that the average particle size of LVP-treated $Rb_6Re_6S_8I_8$ as dissolved in DMF is slightly larger than that of as-prepared $Rb_6Re_6S_8I_8$ without pressure treatment, and significantly larger than that of RbI. The clear discrepancy of average particle sizes among these three specimens suggests that framework and cluster can be preserved within the LVP-treated $Rb_6Re_6S_8I_8$ after dissolution in organic solvent, thereby laying the foundation for all subsequent device fabrication that utilizes the amorphized crystal structure for its permanently enhanced photocurrents.

The detailed device setup with connected probes and interdigitated Pt electrodes optically characterized as shown in Fig. 4f. The

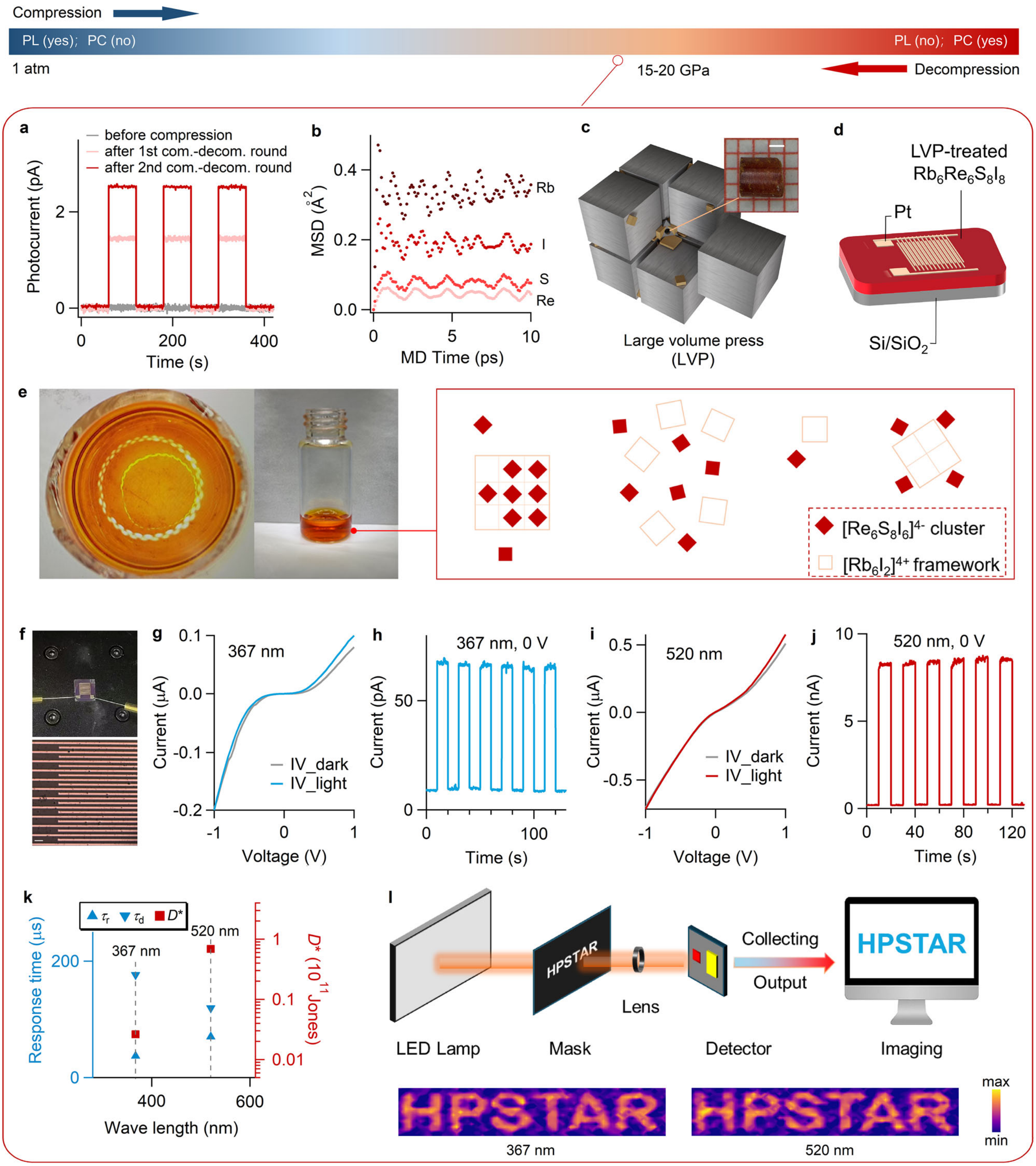

Fig. 4 | Retainable photocurrent at ambience, large-scale sample preparation, and photodetector device. **a** Comparison of ambient on-off photocurrent responses before compression (gray), after first (light red) and second (dark red) compression-decompresion cycles, showing notable generation and increase in the photocurrent after pressure treatments. **b**, Mean squared distances of the Rb, I, S, and Re atoms. The fluctuations stabilized with increasing time in the molecular dynamics simulations. **c** Scheme of the LVP utilized in applying pressure treatment to a large-scale $Rb_6Re_6S_8I_8$ sample. Scale bar, 1 mm. **d** Sketch of a Schottky-type thin-film $Rb_6Re_6S_8I_8$ photodetector device. **e** Good solution processability of the decompressed $Rb_6Re_6S_8I_8$ sample. The optical picture of LVP-treated $Rb_6Re_6S_8I_8$ dissolved in DMF confirmed that the material is dispersible, where the rubidium iodide ($[Rb_6I_2]^{4+}$) framework is stable, rather than behaving as Rb^+ and I^- in DMF. **f** Photograph of the LVP-treated $Rb_6Re_6S_8I_8$-based photodetector device and the on-device interdigitated Pt electrode imaged under a microscope. **g** The I-V curve of devices under 367-nm illumination. **h** On-off photocurrents under 367-nm illumination. **i** The I-V curve of devices under 520-nm illumination. **j** On-off photocurrents under 520-nm illumination. For all tests, no bias voltage is involved, and the devices are self-powered. **k** Response time and specific detectivity (D^*) with both 367 nm and 520 nm illuminations. Here, τ_r and τ_d denote the rise and decay response times, respectively. **l** Schematic diagram of the device ultraviolet and visible imaging device. The photocurrent mappings are observed with the specific pattern obtained by irradiating the device with the "HPSTAR" logo mask using the 367 nm ultraviolet and 520 nm visible lasers. "Max" and "Min" in the color scale denote the relative magnitudes of photocurrent activity. As such, the adoption of LVP in combination with permanent photocurrent generation from high-pressure treatment thus allows practical and scalable device applications.

fabricated self-powered photodetector shows a functional current response within a −1.0 to +1.0 V current-voltage scan under 367 nm (Fig. 4g, h) and 520 nm (Fig. 4i, j) illuminations, demonstrating a large on-off ratio with photocurrent magnitudes of ~60 pA and ~8 nA, respectively. In addition to the fast photocurrent dynamics on the order of 10^2 μs, the detector also exhibits considerable specific detectivity of ~10^{11} Jones (Fig. 4k). Using the photocurrent magnitude as an indicator, we finally achieve highly spatial-resolved red–green-blue (RGB) imaging, in which the word "HPSTAR" is clearly visible (Fig. 4l).

Discussion

We have investigated the photoluminescent to optoelectronic transition occurring in a compressed compound with isolated clusters. Using a combination of high-pressure experiments, we have examined whether such a transition can be retained after the applied pressure was completely released, and found a retention of high-pressure properties, as manifested by the greatly increased photocurrent arising from the initially non-optoelectronic state. These results can guide further applications for the construction of crystalline-amorphous hybrid structures and provide crucial clues regarding the materials that may show high-pressure memory at ambience. In the future, more research is needed to better understand the mechanism by which amorphization leads to the sharp increase in photocurrent, especially on the electronic structure of disorder phase.

Our study also has revealed the potential of pressure treatment in practical applications, enabling the integration of high-pressure-treated materials into functional devices with high-pressure-enhanced performance. Through industrially accessible routes, we have realized large-scale sample preparation and efficient device fabrication of high-performance photodetectors. These results provide a practical demonstration of the feasibility of using pressure-treated materials in real-world optoelectronic applications. To guide future research, we present the following discussion and perspective.

Differences in the rigidity between weakly coupled sublattices is crucial for achieving amorphization upon compression. Pressure-induced amorphization (PIA) can be understood in terms of mechanical collapse (known as the spinodal limit) and a thermodynamically metastable transition, which delimit the upper and lower bounds of this phenomenon[31,32]. In compounds featuring rigid isolated clusters embedded within soft frameworks, applied pressure can markedly reduce the inter-cluster spacing before inducing interactions. However, due to their inherent rigidity, the highly symmetrical clusters impose stringent local symmetry constraints. Consequently, the interplay and balance between these two opposing effects can generate significant shear or other forms of stress, prompting large-scale diffusion of framework atoms and ultimately driving the system into an amorphous state. Such pressure-induced phase transitions have been experimentally observed in compounds characterized by structures comprising isolated polyhedral units such as molybdates[33], tungstates[33], silicides[34], and orthosilicates[35]. We note that a simple soft lattice cannot ensure easy PIA. Pure RbI does not undergo long-range lattice disorder until 67 GPa[36], although it has a bulk modulus on the order of 10.49 GPa[37], which is even slightly lower than that of $Rb_6Re_6S_8I_8$ (~ 11 GPa).

The trade-off between a large sample amount and high pressure achieved is a fundamental and unresolved problem in all pressure-assisted material preparations. Because PIA plays an essential role in discovering exotic and unprecedented material properties under high-pressure conditions, identifying good PIA candidates based on their initial structures is important, because it enables the realization of these properties without the costly use of ultra-high pressure.

Differential sublattice rigidity is also a critical factor for the ambient retention of high-pressure properties. $Rb_6Re_6S_8I_8$ can retain its notable high-pressure photocurrent behavior at ambience because it maintains partial amorphization after full depressurization, exhibiting a thermodynamically metastable and kinetically trapped state. Owing to the relatively weak electrostatic interaction rather than strong chemical bonding between the cluster and framework, upon compression, the framework atoms of Rb and I(2) can deviate from the equilibrium positions to a large extent, thus phenomenologically forming an equipotential surface with small energy variations[32], which provides the basis for multiple metastable states. Then, the relaxation effect, which is useful for understanding the transformations of metastable states, should be analyzed, where the relaxation time is an essential factor in determining the dynamics. In principle, the in-lab decompression process should be much faster than the recovery of materials; otherwise, no irreversibility will be obtained. With the relaxation time (τ) equal to the viscosity (η) divided by the modulus (G_∞), as regulated by Maxwell's expression[38], the soft nature (small modulus) of the Rb-I(2) framework results in a phenomenally large timescale. By contrast, the relaxation time for the Re-S-I(1) cluster, owing to its rigidity, is much shorter. In addition, upon compression, some Rb-I(2) chemical bonds form during amorphization. Regardless of whether these bonds break after depressurization, it is difficult for such a Rb-I(2) framework to rapidly recover to its original lattice positions. In other words, within the weakly interacting cluster-framework sublattices, the hard clusters can restore the order state, whereas the soft and plastic nature of the Rb-I(2) framework leads to a largely extended relaxation time period. Furthermore, the notable steric hindrance effect, which originates from the bulky Re-S-I(1) clusters, impedes the recovery process of Rb-I(2) that must overcome high barriers and has a large timescale. As such, both timescale and spatial effects jointly contribute to the partial amorphization of $Rb_6Re_6S_8I_8$ after pressure treatment, resulting in irreversible structural and property changes.

We further consider the structural characteristics that can facilitate irreversible structural and functional transitions after pressure engineering. Some features, such as the differential sublattice rigidity revealed in this work, structural gradients, including heterojunctions and homojunctions, two-dimensional layered structures with weak interlayer interactions, superlattices, and meticulously designed structural defects, can potentially give rise to both thermodynamic and kinetic discrepancies between various domains in a material, and should be further examined. In addition, it is necessary to consider the time factor, particularly the sample history and the kinetics of compression/decompression, because the generation and conversion of metastable states is a non-traversal process developing under nonequilibrium conditions[39–41].

Methods

Crystals growth

High-quality $Rb_6Re_6S_8I_8$ single crystals were synthesized using the salt flux method[19]. High-purity RbI (99.9%), Re (99.99%), S (99.99%) powders, and I_2 spheres (99.99%) were obtained from Aladdin and combined in a molar ratio of 20:6:8:4 under an argon atmosphere. The mixture was placed in a alumina crucible, which was subsequently sealed in a quartz tube under 10^{-3} Pa. The assembly was then heated to 800 °C for 10 hours and then kept at this temperature for another 10 hours before slowly cooling to 625 °C at 1 $°C \cdot h^{-1}$. Finally, the furnace was turned off, allowing it to cool naturally to room temperature. Through mechanical separation, millimeter-scale orange $Rb_6Re_6S_8I_8$ single crystals were obtained.

Structural characterization at ambient environment

The single-crystal X-ray diffraction data were collected on a Bruker D8 Venture diffractometer equipped with a Mo Kα radiation source ($\lambda = 0.71073$ Å). The structure of $Rb_6Re_6S_8I_8$ was refined using the SHELXL21 refinement package and the Olex2 software package[42,43].

Using Oxford X-Max^N (Oxford Instruments), we obtained morphology and confirmed the chemical composition of $Rb_6Re_6S_8I_8$.

Manufacturing of high-pressure environment

The high-pressure environment was generated using a symmetrical diamond anvil cell (DAC). Pressure calibration was performed using the ruby fluorescence method[44], with mineral oil serving as the pressure-transmitting medium (PTM) unless otherwise specified.

High-pressure synchrotron X-ray diffraction

The crystal structures of $Rb_6Re_6S_8I_8$ under various pressures were determined through in situ synchrotron XRD measurements. Experiments were conducted at beamline 15U of the Shanghai Synchrotron Radiation Facility (SSRF) using a monochromatic X-ray beam focused to dimensions of 11 μm (horizontal) × 3 μm (vertical). Two-dimensional (2D) diffraction patterns were collected and integrated into one-dimensional (1D) data using the Dioptas software package[45]. Structural refinements were performed using the Rietveld method implemented in the General Structure Analysis System-II (GSAS-II) software[46]. The elastic modulus was derived by fitting the experimental data to the third-order Birch-Murnaghan equation of state (Eq. 1)[47]:

$$P(V) = \frac{3B_0}{2}\left[\left(\frac{V_0}{V}\right)^{\frac{7}{3}} - \left(\frac{V_0}{V}\right)^{\frac{5}{3}}\right]\left\{1 + \frac{3}{4}(B' - 4)\left[\left(\frac{V_0}{V}\right)^{\frac{2}{3}} - 1\right]\right\} \quad (1)$$

where V_0 represents the unit cell volume at ambient pressure, determined to be 3757.0(7) Å^3, and B_0 is the bulk modulus, calculated as 11.0(3) GPa. During the fitting process, the first derivative of the bulk modulus, B', was fixed at 12.0. A pair of 300-μm Ia-type diamonds were employed for the measurements.

High-pressure X-ray absorption spectroscopy

X-ray absorption spectra (XAS) at the Re L_3-edge were collected at the ODE beamline of the SOLEIL synchrotron radiation facility. Data were acquired in transmission mode, with energy calibration performed using a standard Re foil as a reference. Data processing and fitting were carried out using the Athena and Artemis software packages[48]. A pair of nano-polycrystalline diamond anvils with a 300-μm culet size were employed. High pressure is generated by squeezing DAC through a membrane device.

High-pressure UV-visible absorption spectra

A custom-designed micro-region spectra system (Gora-UVN-FL, assembled by Ideaoptics) equipped with a Mitutoyo 20× NUV objective was employed to measure UV-visible absorption spectra. A deuterium/halogen light source was used, which provided a wavelength range spanning from 300 nm to 1100 nm. The bandgap of $Rb_6Re_6S_8I_8$ was determined using the Tauc plot method, which is based on the Eq. (2)[49]:

$$\alpha^{1/2} = A\left(h\nu - E_g\right) \quad (2)$$

where α represents the absorption coefficient, hv signifies the photon energy, E_g denotes the bandgap, and A is a proportionality constant. The bandgap value can be accurately determined by plotting $(\alpha hv)^{1/2}$ against hv and extrapolating the linear portion of the curve to the energy axis. The intercept provides the precise bandgap value. For the measurements, a pair of 300-μm IIa-type diamonds were used, with silicone oil serving as the PTM.

High-pressure photoluminescence

Static photoluminescence (PL) spectra were acquired using a 405 nm laser as the excitation source. The emission signals were collected using a NOVA refrigeration spectrometer coupled to a MIcrochrome 5 Pro CMOS detector, with a spectral resolution of 1 nm.

High-pressure time-resolved photoluminescence

For time-resolved PL dynamics measurements, sample was photo-excited by a 405 nm laser diode with a pulse width of 20 ps and a repetition rate of 20 kHz. All PL and time-resolved PL experiments were performed using a modified Mao-type symmetrical diamond anvil cell (DAC) equipped with IIa-type diamond anvils, each with a culet size of 300 μm. For PL imaging, the sample was excited by UV light filtered from a xenon lamp source. Silicone oil was employed as the pressure-transmitting medium (PTM).

High-pressure photocurrent

The high-pressure photocurrent test was conducted on a Keithley 4200A-SCS Parameter Analyzer. A xenon lamp was employed as the simulated visible light source. A symmetrical Sb-type DAC consisting of a pair of 300-μm Ia diamonds was employed. A pre-pressed stainless-steel sheet was drilled with a 280-μm hole, which was subsequently filled with cubic boron nitride (cBN) and subjected to further pressurization. The gasket was then insulated using insulating glue after drilling a 120-μm hole. Two electrodes were fabricated using Pt wires, and the photocurrent was measured under an applied voltage of 3 V for 3 cycles, with each cycle consisting of a 60 seconds light source on period followed by a 60 seconds light source off period.

High-pressure Raman spectra

Raman spectra were acquired utilizing a home-designed low-wavenumber Raman system equipped with a 785 nm laser. The Raman signals were collected by an IsoPlane 320 spectrograph (Princeton Instruments) coupled to a PyLon100BR_eXcelon detector (Princeton Instruments) cooled with liquid nitrogen.

High-pressure middle-infrared transmission spectra

The Bruker vertex 70 v FT-IR spectrometer was employed to measure the MIR transmission spectra. A symmetrical Sb-type DAC consisting of a pair of 200-μm IIa diamonds was used. The transmission signal of the chamber containing silicone oil was collected to serve as a reference signal. $Rb_6Re_6S_8I_8$ (about 5 μm thick) covers the hole, and then the transmission signal was measured under different pressures. The pressure is calibrated by measuring the high-frequency edge of the first-order Raman band at the center of the culet[50].

High-pressure temperature dependence of resistance

The RT curves were measured on physical property measurement system (PPMS, Quantum Design) using a Be-Cu piston-cylinder press containing a pair of 150-μm Ia diamonds. The experimental procedure involved pre-pressing a Be-Cu gasket, drilling a 130-μm hole, filling it with cBN, and subjecting it to further pre-pressing. Afterward, a 65-μm hole was drilled and packed with $Rb_6Re_6S_8I_8$. Four Pt wires were utilized to establish a connection between the copper wires of the external circuit and create a four-electrode configuration. The pressure is calibrated by measuring the high-frequency edge of the first-order Raman band at the center of the culet[50].

First-principles calculation

First-principles calculations were performed within the framework of density functional theory (DFT) using the Vienna Ab Initio Simulation Package (VASP)[51,52]. The exchange-correlation functional was treated using the generalized gradient approximation (GGA) with the Perdew-Burke-Ernzerhof (PBE) parameterization optimized for solids. The valence electron configurations were described by projector augmented wave (PAW) potentials, with the following electronic states included: Rb ($4s^24p^65s^1$), Re ($5d^56s^2$), S ($3s^23p^4$), and I ($5s^25p^5$). A plane-wave basis set with a kinetic energy cutoff of 550 eV was employed, ensuring convergence of the forces on each atom to less than 0.01 electron volt per angstrom. The Brillouin zone was sampled using a Monkhorst-Pack k-point mesh with a spacing of 0.2 Å^{-1}. The electronic band structures are obtained from the refined structures through synchrotron XRD and the Brillouin zones are sampled along high-symmetry points. Infrared intensities and Raman off-resonant activity were calculated using density functional perturbation theory[53–55], respectively. The discrete intensity points are further convolved with the Lorentz function to obtain the spectrum.

The kinetic stabilities are checked by running first-principles molecular dynamic simulation (FPMD). The system is one unit cell, which is consist of 24 Re, 32 I, 24 Rb, and 32 S atoms. We first run equilibrium for 2 picoseconds (ps) at the target *P-T* with the NVT ensemble (constant number of atoms, volume, and temperature). Atomic trajectories were recorded with a time step of 1 fs, and the total simulation time was set to 10 ps for each pressure-temperature (*P-T*) condition. Temperature control was achieved using a Nosé–Hoover thermostat[56]. Pair-distribution function was calculated and averaged from the last 2000 steps of the trajectory. The mean squared displacement is calculated along the trajectory of atomic motions through the Python package Kinisi[57].

Pressurization treatment with large volume press

The $Rb_6Re_6S_8I_8$ powder was compacted into a cylindrical ZrO_2 cavity, which was subsequently incorporated into an Al_2O_3/MgO_2 octahedral structure. This octahedron was centrally situated within a cubic arrangement of eight WC anvils and then placed in the LVP (Kawai-type multi-anvil apparatus, SHTech-2000, Max Voggenreiter). The pressure was systematically increased to 15 GPa over 6 hours, sustained for 2 hours, and then gradually released to ambient pressure within 10 hours.

Fabrication and measurements of photodetector devices

The wafer cleaning process involved sequential treatments with detergent, acetone and isopropyl alcohol, and deionized water for 20 minutes each. Then, the wafers were exposed to UV light for 10 minutes and spin coating was performed in a vacuum glove box. A solution consisting of 15 mg LVP-treated $Rb_6Re_6S_8I_8$ in 1.5 mL N,N-dimethylformamide (DMF) was prepared and spin-coated at 3000 rpm for 30 seconds, and then annealed at 100 °C for 10 minutes before cooling down to room temperature. Subsequently, the Pt electrode was deposited by magnetron sputtering through a mask plate in a vacuum of 9×10^{-4} Pa using a 99.99% Pt target with a device area of 0.5 cm^2. The optoelectronic properties of the prepared devices were characterized using a semiconductor parameter analyzer (Keithley 2400, Tektronix) and light sources with wavelengths of 367 nm and 520 nm. The lighter power density is 50 $mW{\cdot}cm^{-2}$ for both excitations. To determine the response rate, the LED light source was connected to a function generator (TDS2022B, Tektronix) to emit light pulses at different frequencies. In addition, the devices were imaged with specific photocurrent mapping patterns using the assembled imaging system.

Data availability

Data supporting the findings of this work are available within this paper and its Supplementary Information files. Source data are provided with this paper.

References

1. Mao, H.-k & Hemley, R. J. Ultrahigh-pressure transitions in solid hydrogen. *Rev. Mod. Phys.* **66**, 671–692 (1994).
2. Philip, D.-S., Ross, T. H. & Eugene, G. Evidence for a new phase of dense hydrogen above 325 gigapascals. *Nature* **529**, 63–67 (2016).
3. José, A. F.-L. et al. A perspective on conventional high-temperature superconductors at high pressure: Methods and materials. *Phys. Rep.* **856**, 1–78 (2020).
4. Capitani, F. et al. Spectroscopic evidence of a new energy scale for superconductivity in H_3S. *Nat. Phys.* **13**, 859–863 (2017).
5. Kong, L. et al. Simultaneous band-gap narrowing and carrier-lifetime prolongation of organic–inorganic trihalide perovskites. *Proc. Natl Acad. Sci. USA* **3**, 8910–8915 (2016).
6. Tang, H. et al. Toughening oxide glasses through paracrystallization. *Nat. Mater.* **22**, 1189–1195 (2023).
7. Shen, G. & Mao, H.-k High-pressure studies with x-rays using diamond anvil cells. *Rep. Prog. Phys.* **80**, 016101 (2017).
8. Mao, H.-k., Chen, X.-J., Ding, Y., Li, B. & Wang, L. Solids, liquids, and gases under high pressure. *Rev. Mod. Phys.* **90**, 015007 (2018).
9. Mao, H.-k. & Mao, W. Geomimicry—Liberating high-pressure research by encapsulation. *Matter Radiat. Extremes* **7**, 068102 (2022).
10. Tschauner, O. et al. Discovery of davemaoite, $CaSiO_3$-perovskite, as a mineral from the lower mantle. *Science* **374**, 891–894 (2021).
11. Amsler, M., Hegde, V. I., Jacobsen, S. D. & Wolverton, C. Exploring the High-Pressure Materials Genome. *Phys. Rev. X* **8**, 041021 (2018).
12. Zeng, Z. et al. Preservation of high-pressure volatiles in nanostructured diamond capsules. *Nature* **608**, 513–517 (2022).
13. Xiao, T. et al. Nanocrystals with metastable high-pressure phases under ambient conditions. *Science* **377**, 870–874 (2022).
14. Mao, W. & Lin, Y. Making the most of metastability. *Science* **377**, 814–815 (2022).
15. Meng, L. et al. Theoretical and Experimental Advances in High-Pressure Behaviors of Nanoparticles. *Chem. Rev.* **123**, 10206–10257 (2023).
16. Birkhoff, G. Lattice Theory (3rd ed.). *Proc. Am. Math. Soc.* (1967).
17. Sundman, B. O. & Ågren, J. The Sublattice Model. *MRS Online Proc. Libr.* **19**, 115–127 (1982).
18. Singh, S. Phase transitions in liquid crystals. *Phys. Rep.* **324**, 107–269 (2000).
19. Laing, C. C. et al. Solution-processable mixed-anion cluster chalcohalide $Rb_6Re_6S_8I_8$ in a light-emitting diode. *Nat. Mater.* **23**, 230–236 (2024).
20. Gray, T. G., Rudzinski, C. M., Meyer, E. E., Holm, R. H. & Nocera, D. G. Spectroscopic and Photophysical Properties of Hexanuclear Rhenium(III) Chalcogenide Clusters. *J. Am. Chem. Soc.* **125**, 4755–4770 (2003).
21. Shi, W.-Q. et al. Near-unity NIR phosphorescent quantum yield from a room-temperature solvated metal nanocluster. *Science* **383**, 326–330 (2024).
22. Qin, Y., She, P., Huang, X., Huang, W. & Zhao, Q. Luminescent manganese(II) complexes: Synthesis, properties and optoelectronic applications. *Coord. Chem. Rev.* **416**, 213331 (2020).
23. Prüser, H. et al. Interplay between the Kondo effect and the Ruderman–Kittel–Kasuya–Yosida interaction. *Nat. Commun.* **5**, 5417 (2014).
24. Néel, N. et al. Two-site kondo effect in atomic chains. *Phys. Rev. Lett.* **107**, 106804 (2011).
25. Song, K. S. & Williams, R. T. Self-trapped excitons (Springer Series in Solid-State Sciences, **105**, Springer Science & Business Media: Berlin (1996).
26. Liu, G., Kong, L., Yang, W. & Mao, H.-k Pressure engineering of photovoltaic perovskites. *Mater. Today* **27**, 91–106 (2019).
27. Li, S. et al. Self-trapped excitons in all-inorganic halide perovskites: fundamentals, status, and potential applications. *J. Phys. Chem. Lett.* **10**, 1999–2007 (2019).
28. Wang, X. et al. Atomistic mechanism of broadband emission in metal halide perovskites. *J. Phys. Chem. Lett.* **10**, 501–506 (2019).
29. Tomimoto, S. et al. Femtosecond dynamics of the exciton self-trapping process in a quasi-one-dimensional halogen-bridged platinum complex. *Phys. Rev. Lett.* **81**, 417–420 (1998).
30. Brotherton, S. D. *Introduction to Thin Film Transistors: Physics and Technology of TFTs*. Springer International Publishing (2013).
31. Ponyatovsky, E. G. & Barkalov, O. I. Pressure-induced amorphous phases. *Mater. Sci. Rep.* **8**, 147–191 (1992).

32. Machon, D., Meersman, F., Wilding, M. C., Wilson, M. & McMillan, P. F. Pressure-induced amorphization and polyamorphism: Inorganic and biochemical systems. *Prog. Mater. Sci.* **61**, 216–282 (2014).
33. Maczka, M. et al. Pressure-induced structural phase transitions and amorphization in selected molybdates and tungstates. *Prog. Mater. Sci.* **57**, 1335–1381 (2012).
34. Cabrera, R. Q. et al. Pressure-induced structural transformations of the Zintl phase sodium silicide. *J. Solid State Chem.* **182**, 2535–2542 (2009).
35. Nishii, T. et al. X-ray diffraction study of amorphous phase of $BaSi_2$ under high pressure. *Phys. Status Solidi (b).* **244**, 270–273 (2007).
36. Asaumi, K. & Mori, T. High-pressure optical absorption and x-ray-diffraction studies in RbI and KI approaching the metallization transition. *Phys. Rev. B* **28**, 3529 (1983).
37. Kohler, U., Johannsen, P. G. & Holzapfel, W. B. Equation-of-state data for CsCl-type alkali halides. *J. Phys.: Condens. Matter* **9**, 5581–5592 (1997).
38. Dyre, J. C., Olsen, N. B. & Christensen, T. Local elastic expansion model for viscous-flow activation energies of glass-forming molecular liquids. *Phys. Rev. B* **53**, 2171 (1996).
39. Mel'Cuk, A. I., Ramos, R. A., Gould, H., Klein, W. & Mountain, R. D. Long-lived structures in fragile glass-forming liquids. *Phys. Rev. Lett.* **75**, 2522 (1992).
40. Debenedetti, P. G. & Stillinger, F. H. Supercooled liquids and the glass transition. *Nature* **410**, 259–267 (2001).
41. Angell, C. A. Formation of glasses from liquids and biopolymers. *Science* **267**, 1924–1935 (1995).
42. Sheldrick, G. M. Crystal structure refinement with SHELXL. *Acta Crystallogr. C.* **71**, 3–8 (2015).
43. Dolomanov, O. V., Bourhis, L. J., Gildea, R. J., Howard, J. A. K. & Puschmann, H. OLEX2: a complete structure solution, refinement and analysis program. *J. Appl. Crystallogr.* **42**, 339–341 (2009).
44. Mao, H.-k., Xu, J. & Bell, P. M. Calibration of the ruby pressure gauge to 800 kbar under quasi-hydrostatic conditions. *J. Geophys. Res.: Solid Earth* **91**, 4673 (1986).
45. Prescher, C. & Prakapenka, V. B. DIOPTAS: a program for reduction of two-dimensional X-ray diffraction data and data exploration. *High. Press. Res.* **35**, 223 (2015).
46. Toby, B. H. & Von Dreele, R. B. GSAS-II: the genesis of a modern open-source all purpose crystallography software package. *J. Appl. Crystallogr.* **46**, 544 (2013).
47. Katsura, T. & Tange, Y. A simple derivation of the Birch-Murnaghan equations of state (EOSs) and comparison with EOSs derived from other definitions of finite strain. *Minerals* **9**, 745 (2019).
48. Ravel, B. & Newville, M. ATHENA and ARTEMIS: interactive graphical data analysis using IFEFFIT. *Phys. Scr.* **115**, 1007–1010 (2005).
49. Tauc, J. Optical properties and electronic structure of amorphous Ge and Si. *Mater. Res. Bull.* **3**, 37–46 (1968).
50. Akahama, Y. & Kawamura, H. Pressure calibration of diamond anvil Raman gauge to 310 GPa. *J. Appl. Phys.* **100**, 043516 (2006).
51. Perdew, J. P., Burke, K. & Ernzerhof, M. Generalized gradient approximation made simple. *Phys. Rev. Lett.* **77**, 3865–3868 (1996).
52. Perdew, J. P. et al. Restoring the density-gradient expansion for exchange in solids and surfaces. *Phys. Rev. Lett.* **100**, 136406 (2008).
53. Giannozzi, P. & Baroni, S. Vibrational and dielectric properties of C60 from density-functional perturbation theory. *J. Chem. Phys.* **100**, 8537–8539 (1994).
54. Karhánek, D., Bučko, T. & Hafner, J. A density-functional study of the adsorption of methane-thiol on the (111) surfaces of the Ni-group metals: II. Vibrational spectroscopy. *J. Phys.: Condens. Matter* **22**, 265006 (2010).
55. Porezag, D. & Pederson, M. R. Infrared intensities and Raman-scattering activities within density-functional theory. *Phys. Rev. B* **54**, 7830–7836 (1996).
56. Evans, D. J. & Holian, B. L. The Nose-Hoover thermostat. *J. Chem. Phys.* **83**, 4069–4074 (1985).
57. McCluskey, A. R. et al. kinisi-0.6.3., https://github.com/bjmorgan/kinisi (2023).

Acknowledgements

G.L. and H.M. acknowledge support from the Shanghai Key Laboratory of Material Frontiers Research in Extreme Environments (MFree), China (Grant No. 22dz2260800), and the Shanghai Science and Technology Committee, China (Grant No. 22JC1410300). L.K. acknowledges the National Natural Science Foundation of China (Grant No. U2130116). J.G. acknowledges funding from the National Natural Science Foundation of China (Grant No. 52202216), the Natural Science Foundation of Sichuan Province (Grant No. 2023NSFSC0962), and the Focused Research Extended Experience Program of Sichuan University-Pittsburgh Institute. D.W. acknowledges the National Key Research and Development Program of China (Grant No. 2019YFA0705201). X.L. acknowledges the China Postdoctoral Science Foundation (Grant No. GZC20230215) and the National Natural Science Foundation of China (Grant No. 12404001). Q.H. acknowledges the National Natural Science Foundation of China (Grant No. 42150101). Y.G. acknowledges the National Key Research and Development Program of China (Grant No. 2023YFA1406100) and the Double First-Class Initiative Fund of ShanghaiTech University. W.X. acknowledges the Open Project Program of the State Key Laboratory of Surface Physics and Department of Physics, Fudan University (Grant No. KF2022_13), and the Shanghai Sailing Program (Grant No. 23YF1426900). High-pressure XRD characterizations were performed at beamline 15U of the Shanghai Synchrotron Radiation Facility (SSRF). High-pressure XAS measurements were conducted at the ODE beamline of Synchrotron SOLEIL. The authors thank Ms. Yanping Yang, Dr. Junyue Wang, Ms. Xueyan Du, Dr. Zhongli Fan, Ms. Huiru Tian (all from HPSTAR), and Mr. Yunguan Ye (SPST) for their experimental assistance. Special thanks are extended to Dr. Kuo Li (HPSTAR) for insightful discussions.

Author contributions

G.L. supervised the project. J.G. L.K. and G.L. designed the experiments. Z.L., J.G., Z.Z., D.L., Y.W., X.L., S.Z., X.L., Z.Y., M.T., T.X., L.K., H.M., and G.L. analyzed the data. Z.L., X.Z., Z.Y., W.X., J.Y., and Y.G. carried out the crystal synthesis and characterizations at ambient condition. Z.L., Z.Z., D.W., S.Y., L.Z., and Y.D. performed the high pressure XRD measurements and analysis. Z.L., Z.Z., Q.K., N-D.A., K.Z., M.L., N.L., H.D., Z.Z., L.K., W.Y., and G.L. performed the high-pressure XAS measurements and data analysis. Z.L., Z.Z., H.L., and H.S. performed the high-pressure UV-vis absorption spectra, PL, TRPL, Raman spectra, and MIR transmission spectra measurements. Z.L. carried out the high-pressure photocurrent measurements. X.L. and W.Y. performed the high-pressure electrical transport measurements. Q.H. and Y.W. were responsible for the first-principles calculations. Z.L. and Z.Y. performed the LVP treatment. D.L. and D.W. performed the device fabrications. All authors discussed the results and commented on the manuscript.

Competing interests

The authors declare no competing interests.

Inclusion & ethics

This research aligns with the Inclusion & ethical guidelines embraced by Nature Communications.

Additional information

Supplementary information The online version contains supplementary material available at https://doi.org/10.1038/s41467-025-57523-0.

Correspondence and requests for materials should be addressed to Lingping Kong or Gang Liu.

Peer review information *Nature Communications* thanks Y. Charles Cao, Alejandro Goñi and the other anonymous reviewer(s) for their contribution to the peer review of this work. A peer review file is available.

Reprints and permissions information is available at http://www.nature.com/reprints